# Energy cascades in surface semi-geostrophic turbulence

**Yang Zhang [1], Shuwen Zhang [2], and Yakov Afanasyev [3]**

[1]Guangdong Ocean University, Zhanjiang, Guangdong, China
[2]Institute of Marine Science, Shantou University, Shantou, 515063, China
[3]Memorial University of Newfoundland, St. John's, Newfoundland and Labrador, Canada

**Key Points:**

- An asymmetry between cyclonic cold vortices and anticyclonic warm filaments characterizes the surface semi-geostrophic turbulence.
- The ageostrophic component strengthens the forward potential energy cascade by exciting warm filaments but suppresses the inverse kinetic energy cascade by preventing cyclone mergers.
- Horizontal dispersion transforms from a hyper-ballistic regime at small scales to a normal dispersion regime at large scales.

Corresponding author: Yakov Afanasyev, `afanai@mun.ca`

## Abstract

Surface semi-geostrophic turbulence is examined in this study. In our simulations, the strength of the ageostrophic component of the flows is controlled by the Rossby number $\varepsilon$, varying from 0.01 to 0.2. The flows manifest a cyclone-anticyclone asymmetry with a cyclonic preference for cold vortices and an anticyclonic preference for warm filaments. This asymmetry becomes especially pronounced in the flows with large $\varepsilon$, where an abundance of warm filaments is observed. Strong vertical motions concentrate in the small-scale filaments and at the periphery of the vortices. There, the lateral divergence becomes significant. A negative correlation between the divergence and the relative vorticity is identified using joint probability density functions. Slopes of the kinetic and potential energy spectra vary between -2.2 and -1.7 at intermediate scales. Analyses of spectral fluxes demonstrate an inverse kinetic energy cascade and a forward cascade of potential energy. As $\varepsilon$ increases, the filaments become more numerous in the flows. They wrap around cyclones, weakening their interactions and subsequent mergers, thus suppressing the inverse cascade of kinetic energy. We characterize lateral dispersion in the SSG flows using the finite-scale Lyapunov exponents (FSLEs). They are used to identify Lagrangian coherent structures, such as those created by the interaction of vortices. The FSLEs are also used to investigate the regimes of dispersion at different scales. The results show a smooth transition from hyper-ballistic diffusion at small scales to normal diffusion at large scales.



## Plain Language Summary

The generation of submesoscale structures by mesoscale currents is one of the important pathways of energy dissipation in the ocean. It can be modeled with an idealized surface semi-geostrophic (SSG) equations. The SSG model is able to reproduce ageostrophic effects, including a cyclone-anticyclone asymmetry. In this study, we simulate a turbulent SSG flow and demonstrate that, as the ageostrophy increases, warm filaments become more numerous. The filaments contribute to transporting the potential energy towards smaller scales. Meanwhile, the cold cyclones shrink in size and become more isolated from each other due to the shielding by warm filaments wrapping around them. As a result, cyclone interaction and the subsequent mergers are weakened, and the inverse cascade of the kinetic energy towards larger scales is suppressed.


## 1 Introduction

Oceanic turbulence comprises flows of different scales, including ocean-wide gyres, mesoscale eddies, submesoscale eddies, fronts, and filaments. At the lowest end of the scale, submesoscale flows become more familiar due to new evidence provided by field measurements (Shcherbina et al., 2013; Mensa et al., 2018; Pearson et al., 2019; Balwada et al., 2016) and high-resolution numerical simulations (Balwada et al., 2021; Jing et al., 2021). Submesoscale flows are characterized by an O(1) Rossby number and consequently exhibit significant ageostrophy, including large vertical velocity and horizontal divergence (McWilliams, 2016). Thus, they provide a pathway for energy transfer from almost two-dimensional (2D) quasi-geostrophic (QG) turbulence to three-dimensional (3D) turbulence.

Over the years, several theoretical models that go beyond QG but still retain certain physical simplicity—referred to as "intermediate models" in the terminology of McWilliams and Gent (1980)—have been developed. Some of these models exclusively address flows generated by buoyancy perturbations at the surface of the ocean, such as the surface quasi-geostrophic (SQG) model (Blumen, 1978; Held et al., 1994) and the surface semi-geostrophic (SSG) model (Ragone & Badin, 2016). The SQG model has been investigated by different authors (Isern-Fontanet et al., 2006; Klein et al., 2008; Qiu et al., 2016) with respect to its capability to describe upper ocean currents using only surface data, such as

those obtained by satellite altimetry and thermal radiometry. It has been demonstrated that SQG flows generate submesoscale structures (Capet et al., 2008; Carton et al., 2016). Numerical simulations by (Capet et al., 2008) showed that these structures are due to frontogenesis processes, which occur when forward-cascading surface potential energy transfers into inversely-cascading kinetic energy. Spectra of kinetic energy exhibited an approximately -5/3 slope. Similar spectral slopes were obtained from altimetry data by (Traon et al., 2008) and in realistic numerical simulations by (Klein et al., 2008; Chassignet & Xu, 2017). For a comprehensive review of SQG dynamics, readers are referred to (Lapeyre, 2017). The SQG theory relies on the assumption of a small Rossby number, $\varepsilon = U/(f_0 L_D) < 1$, where $U$ is the characteristic velocity scale, $L_D$ is the length scale, and $f_0$ is the Coriolis parameter. However, at submesoscales, $\varepsilon$ can approach or exceed unity (Thomas et al., 2008). Ageostrophic effects become significant at the submesoscale; one example is that strong vortices in the upper ocean are predominantly cyclonic (Shcherbina et al., 2013; Munk, 2000; Griffa et al., 2008). As $\varepsilon$ approaches unity, anticyclones become more vulnerable to frontal instability than cyclones (Hoskins & Bretherton, 1972). Another manifestation of the ageostrophic effects is the vertical motion driven by frontogenesis. It can release the available potential energy of the system, re-stratify the upper ocean, and cause a warming trend at the surface. These features were realized in simulations based on the primitive equations (Roullet & Klein, 2010; Klein et al., 2008).

To include the ageostrophic effects, Hakim et al. (2002) extended the SQG model to the next order of approximation. Their model, called SQG+1, exhibited ageostrophy, including an asymmetry between cold and warm filaments and a preference for cyclonic vortices. However, the SQG+1 model was still constrained by a requirement for a globally small $\varepsilon$. To alleviate this constraint, Ragone and Badin (2016) reformulated the SQG dynamics in a geostrophic coordinate system and proposed a surface semi-geostrophic (SSG) model. The geostrophic coordinate system was previously introduced by Eliassen (1948); Fjørtoft (1962). It is a moving coordinate system that follows the geostrophic current. The total velocity in the advection term is retained rather than being approximated by the geostrophic velocity. SSG simulations by Ragone and Badin (2016) showed features similar to those in the SQG+1 simulations, including a cyclone-anticyclone asymmetry and a surface warming trend. Besides, the SSG simulations demonstrated an improved ability to capture frontogenesis and showed an abundance of small-scale fronts/filaments in the simulated flows due to the improved representation of the nonlinear advection term.

In what follows, we employ the SSG model to investigate the dynamics of surface-intensified flows generated by buoyancy forcing at the surface. The flows are ageostrophic to a significant degree and exhibit frontogenesis and three-dimensional effects. We focus on characterizing vertical velocity and lateral divergence, especially concerning their relation to the relative vorticity and strain rate in filaments and eddies. Spectral characteristics of the flows are also investigated; we go beyond energy spectra and study an energy cascade by computing energy fluxes across the scales. The last objective of this work is a characterization of the Lagrangian dynamics. We compute the finite-size Lyapunov Exponents (FSLEs) to identify the regimes of lateral dispersion at different scales.

In Section 2, we briefly review the SQG and SSG models. Section 3 describes the numerical methods and control parameters employed in this study. The results of the simulations are reported in Section 4, and conclusions are given in Section 5.

## 2 SQG and SSG models revisited

Buoyancy perturbation $b(x, y, z, t) = -g\rho'/\rho_0$, where $g$ is the acceleration due to gravity and $\rho'$ is the density perturbation with respect to the constant reference density $\rho_0$, it is a conserved quantity in both SQG and SSG models. $b$ is related to the (pertur-

bation) geopotential, $\phi = p/\rho_0$, where $p$ is the pressure, via hydrostaticity such that

$$b = \frac{\partial \phi}{\partial z}. \tag{1}$$

The above equation combined with the geostrophic relation

$$f_0(v_g,\ -u_g) = \left(\frac{\partial \phi}{\partial x},\ \frac{\partial \phi}{\partial y}\right), \tag{2}$$

where $f_0$ is the Coriolis parameter, gives the thermal wind equation

$$\left(\frac{\partial b}{\partial x},\ \frac{\partial b}{\partial y}\right) = f_0 \left(\frac{\partial v_g}{\partial z},\ -\frac{\partial u_g}{\partial z}\right). \tag{3}$$

The ocean surface is subject to external heating or cooling. To model this effect, we specify the surface buoyancy perturbation $b_s(x, y)$ at the initial moment $t = 0$ and then allow the flow to evolve freely. Here, the subscript $s$ denotes a surface quantity. It is assumed that $b$ vanishes in the ocean interior at depth $z = -H$, where $H$ is the vertical scale of the motion driven by the buoyancy perturbation. Vertical boundary conditions for the geopotential can then be written as

$$\frac{\partial \phi}{\partial z} = b_s(x, y, t) \quad \text{at} \quad z = 0, \tag{4a}$$

$$\frac{\partial \phi}{\partial z} = 0 \quad \text{at} \quad z = -H. \tag{4b}$$

Note that the background stratification is taken to be linear such that the Brunt-Vaisalla frequency is $N = \text{const}$. The buoyancy perturbation is assumed to remain relatively small such that $N$ remains approximately constant at all times (Hoskins & West, 1979; Ragone & Badin, 2016).

### 2.1 SQG model

Quasi-geostrophic potential vorticity ($q$, PV) remains undisturbed in the interior of the fluid layer at all times such that

$$q = \frac{\partial^2 \phi}{\partial x^2} + \frac{\partial^2 \phi}{\partial y^2} + \frac{f_0^2}{N^2}\frac{\partial^2 \phi}{\partial z^2} = 0. \tag{5}$$

The above equation takes the form of the Laplace's equation

$$\frac{\partial^2 \phi}{\partial x^2} + \frac{\partial^2 \phi}{\partial y^2} + \frac{\partial^2 \phi}{\partial z^2} = 0, \tag{6}$$

when non-dimensionalized using the deformation radius $L_D = NH/f_0$ as the horizontal scale, $H$ as the vertical scale and $U$ as the velocity scale. All quantities in Eq. (6) are dimensionless, but we keep the same notations. Vertical structure of the flow subject to the boundary conditions Eq. (4) can be obtained in the wavenumber space (Tulloch & Smith, 2006)

$$\tilde{\phi}(\boldsymbol{k}, z, t) = \frac{\cosh[(z+1)k]}{k \sinh(k)} \tilde{b}_s(\boldsymbol{k}, t) \tag{7}$$

where the tilde sign denotes the horizontal Fourier transform and $\boldsymbol{k} = (k_x, k_y)$ is the horizontal wavenumber vector whose magnitude is $k = \sqrt{k_x^2 + k_y^2}$. On the surface, $b_s$ is advected by the geostrophic current,

$$\frac{\partial b_s}{\partial t} + J_{xy}(\phi_s, b_s) = 0, \tag{8}$$

where $J_{xy}(A, B) = A_x B_y - A_y B_x$ represents the nonlinear advection term in Jacobian form.

118 ### 2.2 SSG model

As we traverse the scales of the flows from mesoscale down to submesoscale, the Rossby number $\varepsilon$ increases, and the ageostrophic component of velocity becomes significant. To study flows beyond the validity of the quasi-geostrophy, a coordinate system that follows the geostrophic component of the current was introduced (Hoskins & Bretherton, 1972; Hoskins, 1975). The relations between the physical coordinates $(x, y, z)$ and geostrophic coordinates $(X, Y, Z)$ are

$$x = X - \frac{1}{f_0} v_g = X - \frac{1}{f_0^2} \frac{\partial \phi_s}{\partial x}, \tag{9a}$$

$$y = Y + \frac{1}{f_0} u_g = Y + \frac{1}{f_0^2} \frac{\partial \phi_s}{\partial y} \tag{9b}$$

$$z = Z. \tag{9c}$$

In this system, the horizontal advection by the total velocity $(u, v)$ which includes the ageostrophic component, can be expressed using the geostrophic velocity $(u_g,\ v_g)$

$$\frac{D_g}{Dt} = \frac{\partial}{\partial t} + u\frac{\partial}{\partial x} + v\frac{\partial}{\partial y} = \frac{\partial}{\partial t} + u_g\frac{\partial}{\partial X} + v_g\frac{\partial}{\partial Y}. \tag{10}$$

In the geostrophic coordinate system, the Bernoulli function $\Phi = \phi + (u_g^2 + v_g^2)/2$ assumes the role of the geopotential $\phi$ such that

$$\left(\frac{\partial \Phi}{\partial X}, \frac{\partial \Phi}{\partial Y}, \frac{\partial \Phi}{\partial Z}\right) = \left(\frac{\partial \phi}{\partial x}, \frac{\partial \phi}{\partial y}, \frac{\partial \phi}{\partial z}\right) = (f_0 v_g, -f_0 u_g, b). \tag{11}$$

A full set of equations of the SSG model then includes the conservation of buoyancy $b$ and the potential vorticity $q_{sg}$

$$\left(\frac{D_g}{Dt} + w\frac{\partial}{\partial Z}\right) \begin{bmatrix} b \\ q_{sg} \end{bmatrix} = 0. \tag{12}$$

The potential vorticity is defined as:

$$q_{sg} = -\frac{g}{f_0 \rho_0} \boldsymbol{\zeta}_{sg} \cdot \nabla \rho, \tag{13}$$

where the absolute vorticity

$$\boldsymbol{\zeta}_{sg} = \left(-\frac{\partial v_g}{\partial z}, \frac{\partial u_g}{\partial z}, f_0 + \frac{\partial v_g}{\partial x} - \frac{\partial u_g}{\partial y}\right) + \frac{1}{f_0}\left(J_{yz}(u_g, v_g), J_{zx}(u_g, v_g), J_{xy}(u_g, v_g)\right) \tag{14}$$

includes nonlinear terms in the second bracket (Hoskins & Draghici, 1977). In the ocean at rest, $u_g = v_g = 0$, the potential vorticity and the absolute vorticity reduce to their background values:

$$q_{sg} = -\frac{g}{\rho_0}\frac{\partial \rho}{\partial z} = N^2, \tag{15a}$$

$$\boldsymbol{\zeta}_{sg} = f_0 \boldsymbol{k}, \tag{15b}$$

where $\boldsymbol{k}$ is the unit vector in the vertical direction. In the presence of the flow, the vertical component of the absolute vorticity,

$$\boldsymbol{\zeta}_{sg} = [f_0 + \frac{\partial v_g}{\partial x} - \frac{\partial u_g}{\partial y} + \frac{1}{f_0} J_{xy}(u_g, v_g)]\boldsymbol{k}. \tag{16}$$

remains dominant. The reciprocal of the Jacobian of a transformation from physical to geostrophic coordinates may be written as (Hoskins, 1976)

$$J_g^{-1} = \frac{f_0}{\zeta_{sg}} = 1 - \frac{1}{f_0^2}\left(\frac{\partial^2 \Phi}{\partial X^2} + \frac{\partial^2 \Phi}{\partial Y^2}\right) + \frac{1}{f_0^4}\left[\frac{\partial^2 \Phi}{\partial X^2}\frac{\partial^2 \Phi}{\partial Y^2} + (\frac{\partial^2 \Phi}{\partial X \partial Y})^2\right]. \tag{17}$$

and $q_{sg} = \zeta_{sg}/f_0\Phi_{zz}$. An assumption of negligible potential vorticity in the fluid interior leads to a nonlinear Monge-Ampére equation:

$$\frac{1}{N^2}\frac{\partial^2\Phi}{\partial Z^2} + \frac{1}{f_0^2}\left(\frac{\partial^2\Phi}{\partial X^2} + \frac{\partial^2\Phi}{\partial Y^2}\right) - \frac{1}{f_0^4}\left[\frac{\partial^2\Phi}{\partial X^2}\frac{\partial^2\Phi}{\partial Y^2} + \left(\frac{\partial^2\Phi}{\partial X\partial Y}\right)^2\right] = 0. \tag{18}$$

The above equation replaces the linear Laplace's equation Eq. (6) in the SQG model. To solve Eq. (18) we follow a numerical technique developed by Ragone and Badin (2016). For further details, readers are referred to Appendix A.

## 3 Numerical method

The model domain is discretized in the geostrophic space $(X, Y, Z)$. The domain is periodic in both horizontal directions and contains $N_x = 512$ grid points in each direction. The non-dimensional horizontal domain size is set to $L/L_D = 6$, where $L$ is the dimensional horizontal domain size, and $L_D$ is the deformation radius. This results in a non-dimensional horizontal grid size of approximately $\Delta X \approx 0.01$. In the vertical direction, the domain is bounded by rigid walls and contains $N_z = 20$ levels which are spaced exponentially with the majority of grid points close to the top surface.

To initialize the simulation, an initial surface buoyancy perturbation $b_s(X, Y, t = 0)$ is specified in wavenumber space

$$\tilde{b}_s(\boldsymbol{k}, t = 0) = A\frac{k^{m/4}}{(k + k_0)^{m/2}} \tag{19}$$

Here, we follow (Hakim et al., 2002; Ragone & Badin, 2016) taking $m = 20$ and $k_0 = 14$ and assigning a random phase to each mode $\boldsymbol{k}$ such that the random initial field can have a prescribed spectrum structure. The amplitude $A$ is tuned such that the initial RMS velocity is fixed at 1 m/s for all our simulations; this velocity magnitude is typical for oceanic fronts (Gula et al., 2016).

Eq. (A9) is integrated in time using the 4th-order Runge-Kutta scheme. The nonlinear Jacobian $J_{XY}$ is discretized in the $(X, Y)$ plane using (Arakawa, 1966)'s scheme, which conserves both the kinetic energy and enstrophy. Then, it is transformed into the $(k_X, k_Y)$ space for the time integration. This semi-pseudo scheme was shown to be able to capture the development of sharp fronts (Constantin et al., 2012). To remove the aliasing errors introduced by the nonlinearity, $\tilde{b}_s(\boldsymbol{k}, t)$ is multiplied by a low-pass filter (Hou & Li, 2007):

$$\exp[-\alpha(|\frac{k_X}{k_{nq}}|^\beta + |\frac{k_Y}{k_{nq}}|^\beta)] \tag{20}$$

where $k_{nq} = \pi/\Delta X$ is the Nyquist wavenumber and $\alpha = 512$ and $\beta = 20$ as in (Ragone & Badin, 2016). Not unlike the Orszag 2/3 cutoff, this exponential filter suppresses the highest 1/3 wavenumbers. Moreover, it can capture extra 15% more effective wavenumbers than the Orszag 2/3 cutoff, thus providing a better representation for the small-scale structures.

Substituting the updated $b_s(\boldsymbol{k}, t)$ into Eq. (A7) we obtain $\tilde{\Phi}(\boldsymbol{k}, Z, t)$ at the next time step; its vertical derivative gives $\tilde{b}(\boldsymbol{k}, Z)$. To obtain $b_s(X, Y, Z)$ and $\Phi(X, Y, Z)$ in the geostrophic coordinates, an inverse Fourier transform in the horizontal plane at each depth is performed. The flow is then transformed into the physical space $(x, y, z)$ using a fixed-point iteration method (Ragone & Badin, 2016).

Six simulations were performed where the characteristic Rossby number $\varepsilon$ was varied between 0 and 0.2. Note that when $\varepsilon = 0$, the SSG solution Eq. (A7) reduces to the SQG solution Eq. (7). In that case, the geostrophic coordinate system becomes identical to the physical coordinate system, and no coordinate transformation is needed. Non-dimensional surface buoyancy, $b_s$, and time, $T$, can be restored to their dimensional form using factors $NU$ and $(\varepsilon f_0)^{-1}$, respectively.

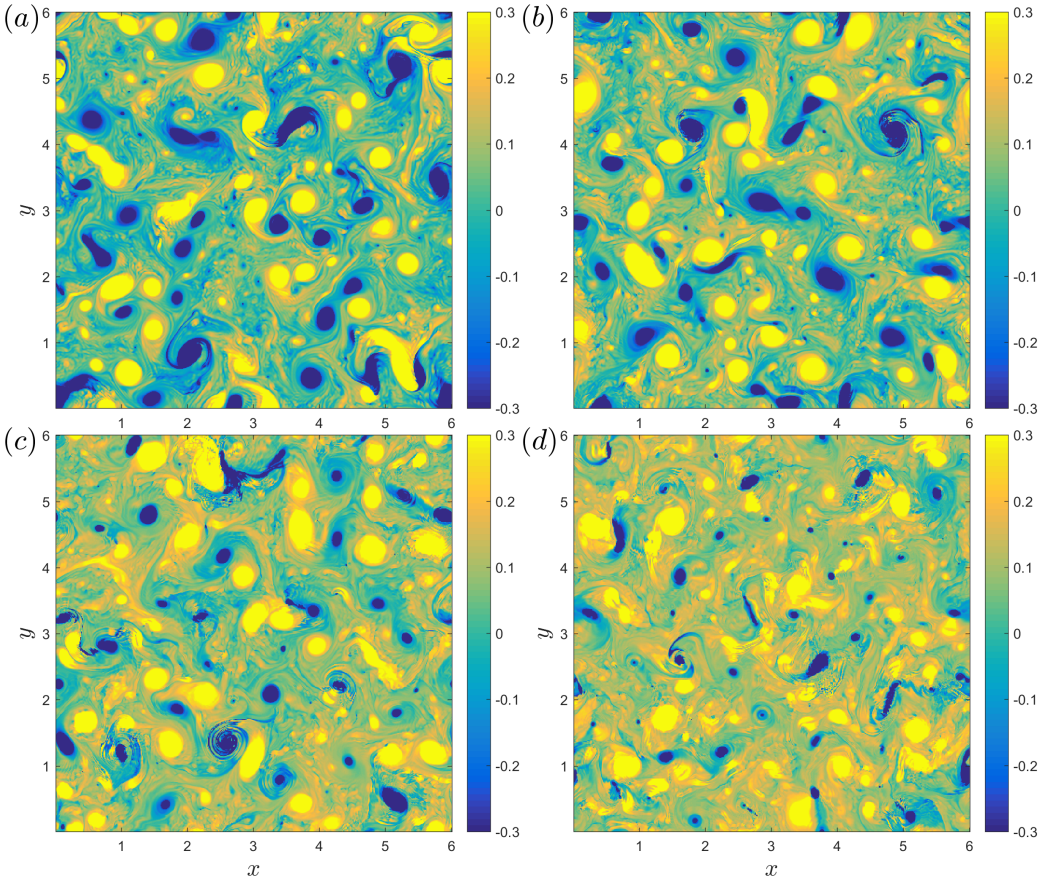


**Figure 1.** (Colour online) Surface buoyancy $b_s(x, y)$ in the simulations with $\varepsilon = 0.05$ (a), 0.1 (b), 0.15 (c), and 0.2 (d) at $T = 50$.

# 4 Results

## 4.1 Flow evolution

We restrict our analyses to an early-time evolution of the SSG flows when there is an abundance of small-scale filaments and vortices with strong nonlinear interactions.

Figure 1 shows the buoyancy $b_s$ at the surface captured at $T = 50$ in simulations with different $\varepsilon$. Patches of cold (blue color) water induce cyclonic vortices, while warm patches (yellow color) induce anticyclones. Numerous filaments fill the area between the vortices. The filaments are embedded in strong shear and are unstable; they roll into smaller vortices. When $\varepsilon$ is relatively small, the cyclones and anticyclones populate the flow field in approximately equal numbers (Fig. 1(a) and (b)). As $\varepsilon$ increases, the cold cyclones in Fig. 1(c) shrink in size while warm anticyclonic vortices expand. This effect is a manifestation of the pressure terms in the coordinate transform (second equality in Eq. (9)(a) and (b)) and is due to the lateral divergence and convergence of the velocity (Hoskins, 1975). The area between coherent vortices is now filled with predominantly warm filaments (Fig. 1(d)). Their accumulation at the surface results in a warming trend with increasing $\varepsilon$. Similar scenarios have been shown previously in the simulations by (Ragone & Badin, 2016; Hakim et al., 2002). They pointed out that the preference for cold cyclones and the dominance of warm filaments are due to the inclusion of the ageostrophic component.

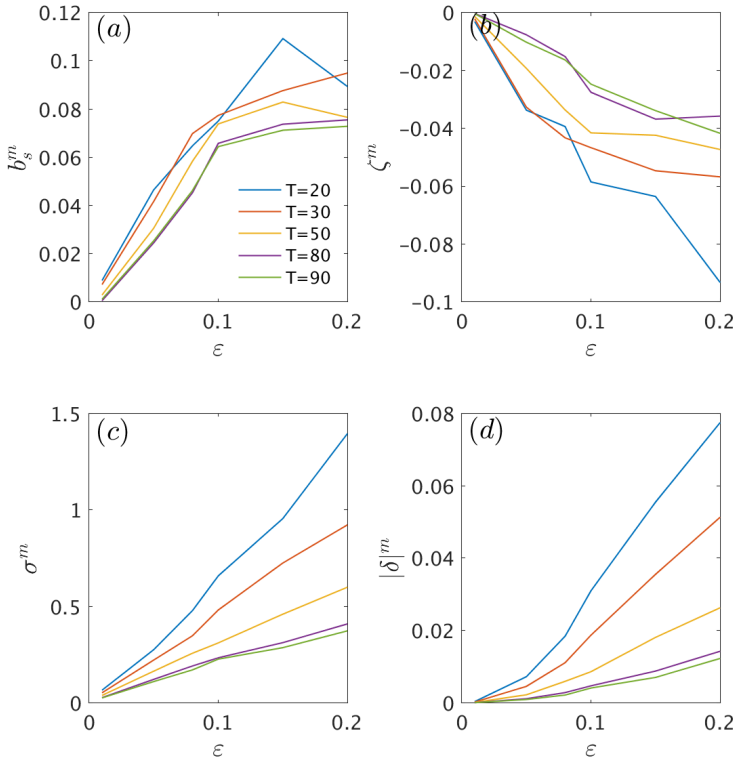


**Figure 2.** (Colour online) The median values for surface buoyancy perturbation $b_s^m$(a), relative vorticity $\zeta^m$(b), strain rate $\sigma^m$ (c), and absolute horizontal divergence $|\delta|^m$(d) as functions of $\varepsilon$ at different times.

The median value of $b_s(x,y)$ versus $\varepsilon$ at different times is shown in Fig. 2(a). When $\varepsilon = 0.01$, the high-order ageostrophic correction term in Eq. (A7) the SSG model is negligible, and the SSG flow becomes indistinguishable from the SQG flow. The distribution of cyclones and anticyclones becomes symmetric and the median value of the surface buoyancy perturbation, $b_s^m$, is close to zero. As $\varepsilon$ increases, $b_s^m$ shifts to positive values. It corresponds to the surface warming shown in Fig. 1(c,d). The warming effect decreases with time as the flows decay.

Accumulation of warm water at the surface leads to a general anticyclonic circulation, such that the median value of the relative vorticity becomes negative, $\zeta^m < 0$, Fig. 2(b). Here the (vertical component of) relative vorticity is $\zeta = \partial v/\partial x - \partial u/\partial y$. This mean anticyclonic circulation strengthens as $\epsilon$ increases. The median value of the strain rate $\sigma^m$ also increases with $\epsilon$ because of the enhanced stirring created by the abundant small-scale filaments and vortices, Fig. 2(c). Here the strain rate is defined as:

$$\sigma = \left[ \left( \frac{\partial v}{\partial x} + \frac{\partial u}{\partial y} \right)^2 + \left( \frac{\partial u}{\partial x} - \frac{\partial v}{\partial y} \right)^2 \right]^{1/2}. \tag{21}$$

Since vertical motions concentrate in these small-scale structures (Fig. 3(b)) where the local convergence/divergence is large, the median value of the lateral divergence, $|\delta|$, also increases with $\varepsilon$ (Fig. 2(d)).

Oceanic fronts are characterized by a relatively large vertical velocity of approximately 1 mm/s (Mahadevan & Tandon, 2006; McWilliams, 2016; Ruiz et al., 2019). In the SSG model, vertical velocity can be diagnosed by solving the so-called "Ω-equation" (Hoskins & West, 1979). An analytical solution of the "Ω-equation" in the wavenumber space is given in Appendix B. Vertical velocity fields right below the surface at $z = -0.1$ are shown in Fig. 3 for two simulations with different $\varepsilon$. In vortices, vertical velocity appears as a quadrupolar structure Fig. 3(a). In filaments, positive and negative stripes of $w$ are created. At larger $\varepsilon$, the magnitude of $w$ increases; the difference between Fig. 3(a) and (b) is approximately one order of magnitude. Vertical motions become concentrated at the periphery of vortices and the bands of upwelling ($w > 0$, yellow color) become stronger than the bands of downwelling ($w < 0$, blue color).

Vertical profiles of $w(x,y)$ (not shown here) show that the magnitude of $w(x,y)$ is maximum in a subsurface layer at $z_{max} \approx -0.1$. Below this level, $w(x,y)$ decays monotonically with depth. Vertical derivative of $w$ is related to the lateral divergence of velocity, $\delta$, as:

$$\delta = \frac{\partial u}{\partial x} + \frac{\partial v}{\partial y} = -\frac{\partial w}{\partial z}. \tag{22}$$

Since $w$ vanishes at the surface, the lateral divergence can be approximated as $\delta \approx w(z_{max})/z_{max}$.

Fronts/filaments are associated with strong buoyancy gradients in the cross-front direction and strain-dominated confluent flows which act to enhance the gradients. In an elongated front where the variation of velocity in the along-front direction is negligible, $\delta$ is related to the relative vorticity, $\zeta$, and the rate-of-strain, $\sigma$ as:

$$\delta^2 = \sigma^2 - \zeta^2. \tag{23}$$

The relation between these quantities was previously discussed for oceanic and numerical flows by (Shcherbina et al., 2013; Chavanne et al., 2010; Balwada et al., 2020; Maalouly et al., 2023). Chavanne et al. (2010) reported a negative linear correlation between $\delta$ and $\zeta$ for an oceanic front during an active phase of its evolution. Their observation is in agreement with the prediction by (Hoskins & Bretherton, 1972) that $\delta \propto -\bar{\sigma}\zeta$ where $\bar{\sigma}$ is the large-scale strain rate. Thus, cyclonic circulations in a strain field create lateral convergence while anticyclonic ones create lateral divergence. To obtain a $\zeta - \delta$ relation for our flows, we computed the joint probability density function (PDF) in the two-dimensional

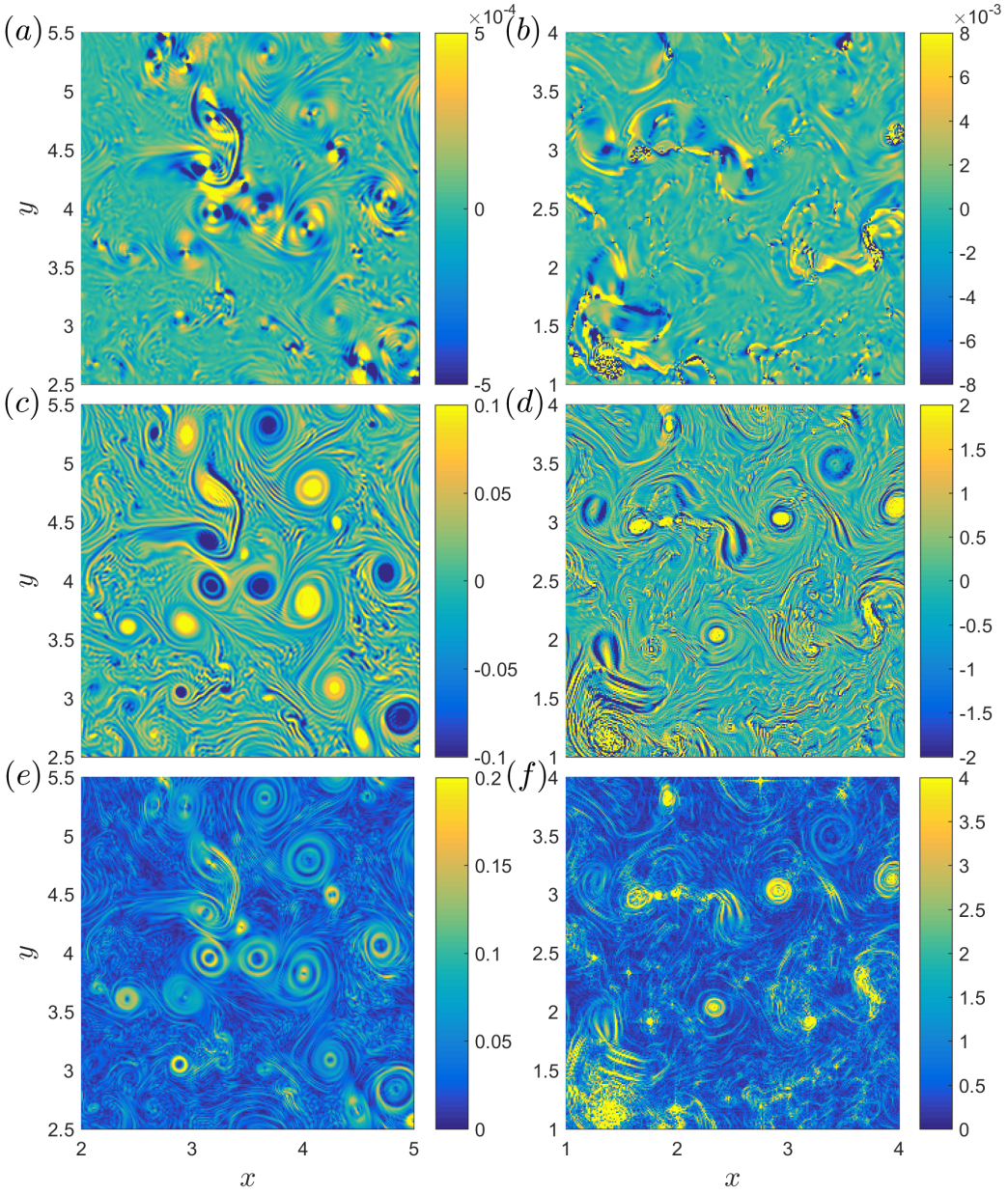


**Figure 3.** (Colour online) Vertical velocity $w(x, y)$ at $z = -0.1$ (a, b), normalized relative vorticity $\zeta/f_0$ (c, d), and normalized strain rate $\sigma/f_0$ (e, f) for the flows with $\varepsilon = 0.01$ (left column) and $\varepsilon = 0.2$ (right column) at $T = 50$.

parameter space spanned by $\zeta$ and $\delta$. $\zeta$ and $\delta$ were normalized by the Coriolis parameter $f_0$, they were then sorted according to their normalized values into bins of size 0.01 by 0.01. After that, the joint PDF can be obtained by counting the number of occurrences when $\zeta(x, y)$ and $\delta(x, y)$ drop into each bin. Finally, the joint PDFs were temporally averaged over a period from $T = 45$ to $T = 55$.

Figure 4(a) shows that the joint PDF of $\zeta$ and $\delta$ is aligned along a straight line with a negative slope. White dashed line in Fig. 4(a) is $\delta = -\frac{1}{2}\bar{\sigma}\zeta$, where $\bar{\sigma} = 0.04$ is the spatial mean of $\sigma$ averaged over the parameter region where PDF$> 3$; $\bar{\sigma}$ represents a typical value of the large-scale strain rate. This relation was previously proposed in (Davies & Muller, 1988; Lapeyre & Klein, 2006b) for the surface-intensified currents decaying exponentially with depth, which is consistent with the SSG model employed here.

Fig. 4(b) shows the joint PDF in the $\zeta-\sigma$ parameter space. The PDF is aligned along the lines $\sigma = \pm\zeta$, which indicates a pure shear relationship. This also suggests that a contribution of $\delta$ in Eq. (23) is small.

To show the relation between $\delta$, $\sigma$, and $\zeta$ in a single diagram, we computed $\delta$ averaged over each bin in the $\zeta-\sigma$ parameter space. This procedure gives a conditional-mean lateral divergence shown in Fig. 4(c). Note that this diagram can also be interpreted in terms of vertical velocity in the subsurface layer. Strong divergence/upwelling (yellow color) is mainly associated with anticyclonic vorticity while convergence/downwelling (blue color) is associated with the cyclonic vorticity in the strain-dominated areas located above the line $\sigma = |\zeta|$. In the vorticity-dominated areas below the line $\sigma = |\zeta|$, the divergence is generally of the same sign as vorticity, opposite to that in the strain-dominated areas. However, the signal there is weaker and noisier than that in the strain-dominated areas. Note that according to a frontogenesis model by Barkan et al. (2019) the three quantities in Eq. (23) are of the same order of magnitude in a submesoscale front. In our simulations, this can be locally satisfied in strong filaments. High levels of $\delta$ create graininess in Fig. 4 (c).

### 4.2 Spectral characteristics

Kinetic and potential energy spectra at depth $Z$ are defined as

$$\mathcal{K}(\boldsymbol{k}, Z) = k^2\tilde{\Phi}(\boldsymbol{k}, Z)\tilde{\Phi}^*(\boldsymbol{k}, Z), \tag{24a}$$

$$\mathcal{P}(\boldsymbol{k}, Z) = \tilde{b}_s(\boldsymbol{k}, Z)\tilde{b}_s^*(\boldsymbol{k}, Z), \tag{24b}$$

where $\boldsymbol{k} = (k_x, k_y)$ and the superscript $*$ denotes the complex conjugate. One-dimensional (1D) spectra $K(k, Z)$ and $P(k, Z)$ are computed by averaging the above equations over the azimuthal angle $\theta = \tan^{-1}(k_y/k_x)$ in the wavenumber space. Fig. 5 shows 1D kinetic energy spectra $\mathcal{K}_s(k)$ and $P_s(k)$ for the flows at the surface at different $\varepsilon$. At larger $\varepsilon$, the fraction of total kinetic or potential energy at smaller scales (larger $k$) increases while the fraction at larger scales (smaller $k$) decreases. This shift in the energy distribution across scales is a manifestation of abundant and energetic small-scale features including filaments at larger $\varepsilon$. As a result, the spectral slope becomes less steep at larger $\varepsilon$; it varies between -2.2 and -1.7 for both $\mathcal{K}_s$ and $\mathcal{P}_s$ for $\varepsilon$ varying between 0.01 and 0.2. A middle point of this spectral seesaw is at approximately $k = 20$.

Previously, Ragone and Badin (2016) made an observation that energy accumulation at small scales strongly depends on $\varepsilon$. However, their -3 slope of $\mathcal{K}_s$ was steeper than the -2 slope in our flows. This difference might be due to the fact that their analyses were performed at a later time $T = 100$ when the flow is dominated by the long-lived coherent vortices rather than filaments. The presence of these vortices could steepen the spectral slope. In our case, the nonlinear interactions are strong at $T = 30$ and filaments are abundant. A similar -2 slope was previously measured during an early stage of the SQG flow simulation by (Capet et al., 2008).

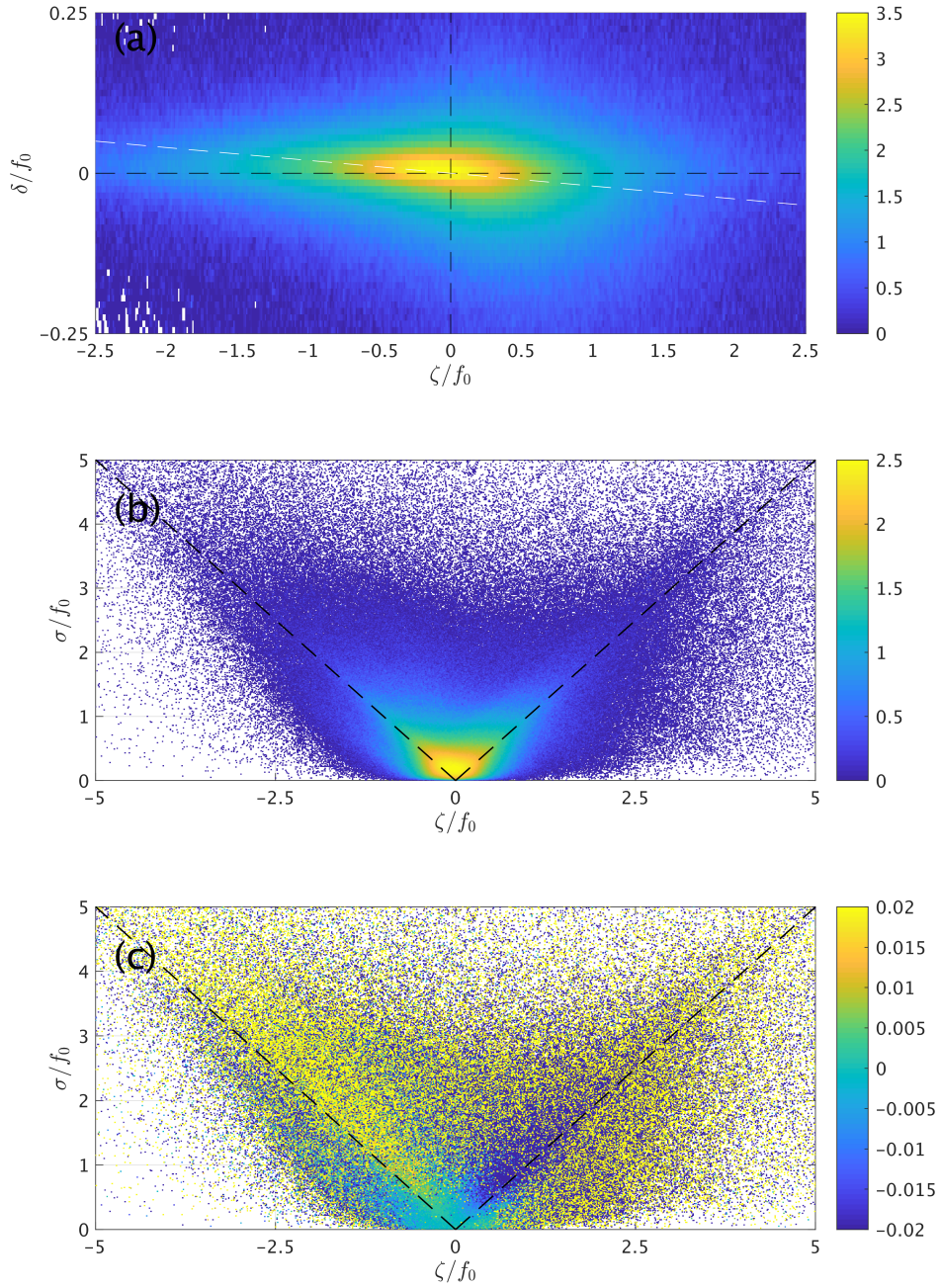


**Figure 4.** (Colour online) Joint PDF in the $\zeta$-$\delta$ parameter space (a); that in the $\zeta$-$\sigma$ parameter space (b); and $\delta/f_0$ conditioned in the $\zeta$-$\sigma$ parameter space (c) for the flow with $\epsilon = 0.2$. The color scales are logarithmic and areas with zero PDF are left blank. White dashed line in (a) corresponds to $\delta = -\bar{\sigma}/2\zeta$. Black dashed lines in (b) and (c) correspond to $\sigma = \pm\zeta$.

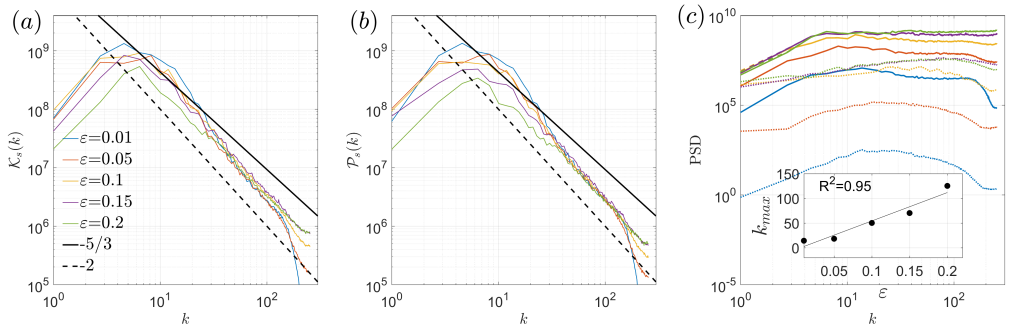


**Figure 5.** (Colour online) One-dimensional kinetic energy spectra $\mathcal{K}_s(k)$ (a) and potential energy spectra $\mathcal{P}_s(k)$ (b) for the flows with $\varepsilon$ varying between 0.01 and 0.2 at $T = 30$. The solid, dotted, and dashed curves in panel (c) show the one-dimensional PDS for $\tilde{\zeta}(k)$, $\tilde{\delta}(k)$, and $\tilde{\sigma}(k)$, respectively. Note that $\tilde{\sigma}(k)$ is dominated by $\tilde{\zeta}(k)$, the dashed lines coincide with the solid ones. The insert shows the wavenumber $k_{max}$ for the peak in $\tilde{\delta}(k)$, where a linear fit is shown by the straight line.

Boyd (1992) investigated spectral characteristics of a one-dimensional front using the Burger's equation $u_t + uu_x = 0$. He showed that the kinetic energy spectrum of the solution follows a $k^{-2}$ scaling law shortly after the formation of the front. We believe that the approximately -2 slope in Fig. 5 is due to the nonlinear advection term in Eq. (A9). At later times, when filaments are getting destroyed in the strain field of coherent vortices, a -3 or even steeper spectral slope emerges in all of our simulations (not shown here). An approximately -5/3 slope is observed at larger $\varepsilon = 0.15,\ 0.2$. This result is in agreement with that of the simulations by Ragone and Badin (2016) and with the theoretical result by (Blumen, 1978) who predicted the -5/3 slope for an inertial range of the potential energy.

Comparison of Fig. 5 (a) and (b) shows that the slopes of $\mathcal{P}_s(k)$ are approximately equal to those of $\mathcal{K}_s(k)$. This feature was also observed in the SQG flows in an infinitely deep ocean (Lapeyre & Klein, 2006a). In that case, the SQG solution Eq. (7) becomes

$$\tilde{\phi}(\boldsymbol{k}, z, t) = \frac{1}{k}\tilde{b}_s(\boldsymbol{k}, z)\exp(-kz) \tag{25}$$

Substitution of the above equation into Eq. (24) shows that

$$\mathcal{P}_s(\boldsymbol{k}) = \mathcal{K}_s(\boldsymbol{k}) \tag{26}$$

is satisfied at the surface $z = 0$. Our computations suggest that this result is also valid for the SSG flows.

To assess the spectral characteristics of the small-scale filaments we computed the power spectral density (PSD) for the gradient fields, namely the relative vorticity $\zeta$, lateral divergence $\delta$ and strain rate $\sigma$, Fig. 5(c). An approximately flat ("white") spectrum is observed in the wavenumber range where the kinetic energy slope is about $-2$. The almost geostrophic flow ($\varepsilon = 0.01$) is non-divergent such that $\tilde{\delta}(k)$ is negligible (dotted blue curve) and the PSD of $\tilde{\zeta}$ and $\tilde{\sigma}$ (solid and dashed blue curves) are almost identical. Although $\tilde{\delta}$ increases significantly with $\varepsilon$ it remains much smaller than $\tilde{\zeta}$ or $\tilde{\sigma}$. At larger $\varepsilon$, the flat spectrum extends to higher wavenumbers due to the growing contribution of small-scale energetic filaments. An inset in Fig. 5(c) shows the wavenumber $k_{max}$ at which the maximum magnitude of $\tilde{\delta}(k)$ is reached. $k_{max}$ can be considered as a characteristic wavenumber of submesoscale filaments in our flows. It grows approximately

linearly with $\varepsilon$ (thick-black line). This is a consequence of the linear dependence of the high-order correction term in Eq. (A7), which determines the lateral divergence, on $\varepsilon$.

Energy spectra are sustained by transfers of energy across the scales, an energy cascade. However, the spectra themselves do not allow us to determine the magnitude or the direction of the cascade. The investigation of the cascades requires a different approach. Here we employ the spatial filtering technique developed by (Germano, 1992; Chen et al., 2006; Aluie et al., 2018) and used in previous studies of rotating shallow-water and baroclinic turbulence (Afanasyev & Craig, 2013; Zhang & Afanasyev, 2016). Fluxes of the kinetic energy and the potential energy are defined as:

$$\Pi_u^l(x,y) = -[(v_i v_j)^l - v_i^l v_j^l]\frac{\partial v_i^l}{\partial x_j}, \tag{27a}$$

$$\Pi_b^l(x,y) = -[(v_j b)^l - v_j^l b^l]\frac{\partial b^l}{\partial x_j}, \tag{27b}$$

where $v_i$ is the $i$th component of the horizontal velocity, and summation over repeated indices is implied. The superscript $l$ denotes a spatial scale. $\Pi_u^l$ and $\Pi_b^l$ are computed using low-pass filtering which is performed by convolving the correspondent fields with a Gaussian kernel $G(l) = 9/(2\pi l^2)\exp(-9r^2/2l^2)$. Positive values of $\Pi_u$ or $\Pi_b$ indicate a forward cascade, i.e., energy transfers from larger to smaller scales while negative values indicate the cascade in the opposite direction, the inverse cascade. The cut-off scale $l$ can be related to the non-dimensional wavenumber as $k = 2\pi/l$.

Figure 6 shows $\Pi_u^l(x,y)$ and $\Pi_b^l(x,y)$ computed for two wavenumbers $k = 85$ and $k = 18$. At the larger wavenumber, both kinetic and potential energy fluxes are concentrated predominantly along filaments and at the periphery of the vortices. Positive and negative fluxes alternate; both forward and inverse energy transfers are present. Note that $\Pi_u^l$ is relatively small at $k = 85$ in Fig. 6 (a). The potential energy flux in Fig. 6 (b) is of a quadrupolar structure around vortices while in the filaments away from the vortices, it is mainly positive. At the smaller wavenumber, the fluxes are mainly concentrated within vortices and are quadrupolar Fig. 6 (c) and (d). Note that the quadrupolar structure of energy fluxes was observed in numerical simulations by Xiao et al. (2009) as well as in laboratory experiments by Afanasyev and Craig (2013). The quadrupolar structure appears to be due to vorticity gradient stretching by strain fields Kimura and Herring (2001). Interestingly, the kinetic energy flux appears to be concentrated in intense cold cyclones (Fig. 6 (c)) while the potential energy flux reaches its largest magnitude in warm anticyclones (Fig. 6 (d)).

When both positive and negative fluxes are present in the flow, the overall direction of the energy cascades can be revealed by spatial averaging over the flow domain. Figure 7 shows mean fluxes $\bar{\Pi}_u$ and $\bar{\Pi}_b$ versus wavenumber $k$ for simulations with varying $\varepsilon$. The kinetic energy flux is negative across the entire range of wavenumbers which indicates the energy transfers to larger scales, an inverse cascade. Maximum magnitudes of the flux are achieved at $k \approx 18$ Figure 7(a); the overall magnitude of the flux decreases with increasing $\epsilon$. This decrease is most likely caused by the joint effect of the ageostrophic correction term in Eq. (A8) and the coordinates transform Eq. (9). When $\varepsilon$ increases the cyclones become smaller and separated farther away from each other; their mergers then become less likely. Potential energy cascades forward at all wavenumbers above $k \approx 20$ (Fig. 7(b)). Maximum values of $\bar{\Pi}_b$ are achieved at $k \approx 85$ and the magnitude of the flux increases with increasing $\varepsilon$. Since the potential energy flux mainly occurs at large wavenumbers, it is clearly related to small-scale elements of the flows including cyclones and filaments. These elements become more abundant and energetic with increasing $\varepsilon$.

To further explore the relation between the flux of potential energy with the velocity field we plotted the isolines of $\Pi_b^l(x,y)$ computed at $k = 85$ together with the vertical velocity field, $w$, just below the surface (at $z = -0.01$) (Fig. 8(a)). $w$ appears to be positively correlated with $\Pi_b^l(x,y)$; filaments formed by upwelling water are associ-

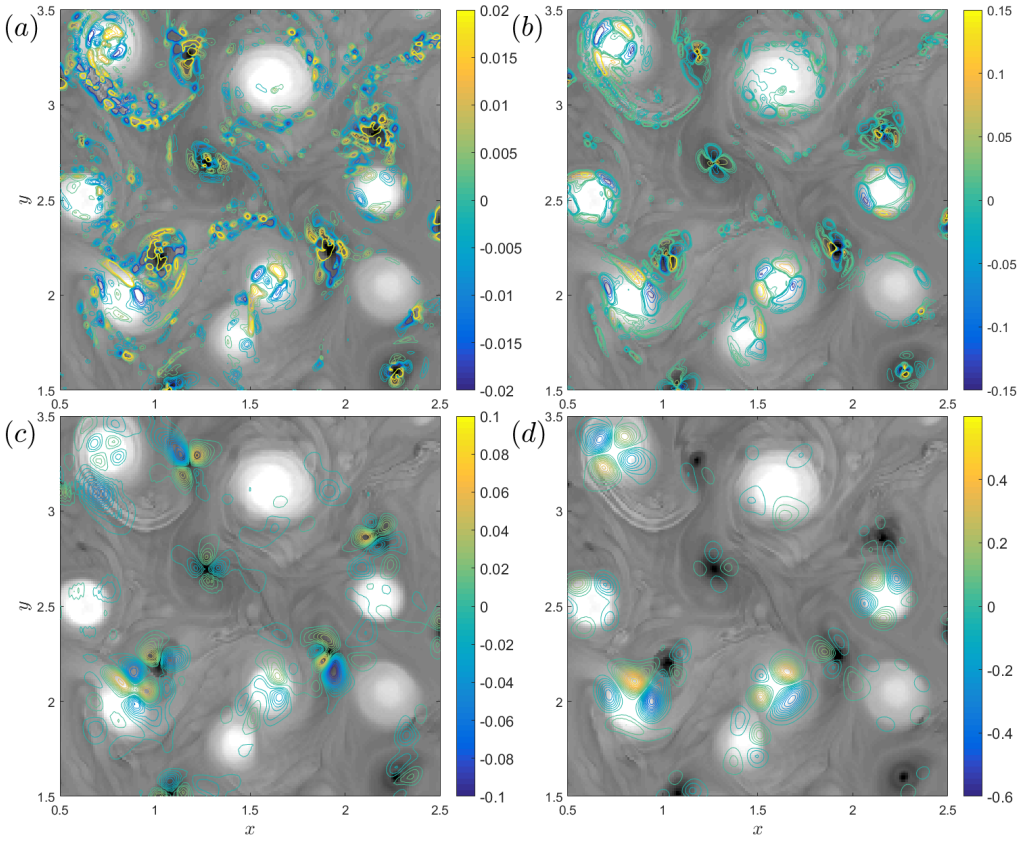


**Figure 6.** (Colour online) Kinetic energy flux $\Pi_u^l(x,y)$ (a, c) and potential energy flux $\Pi_b^l(x,y)$ (b, d) for the surface flow with $\varepsilon = 0.1$ at $T = 30$(contours). The fluxes are across the wavenumbers $k = 85$ (top row) and $k = 18$ (bottom row). Gray-scale background shows the surface buoyancy in the range between -1.2 and 1.2.

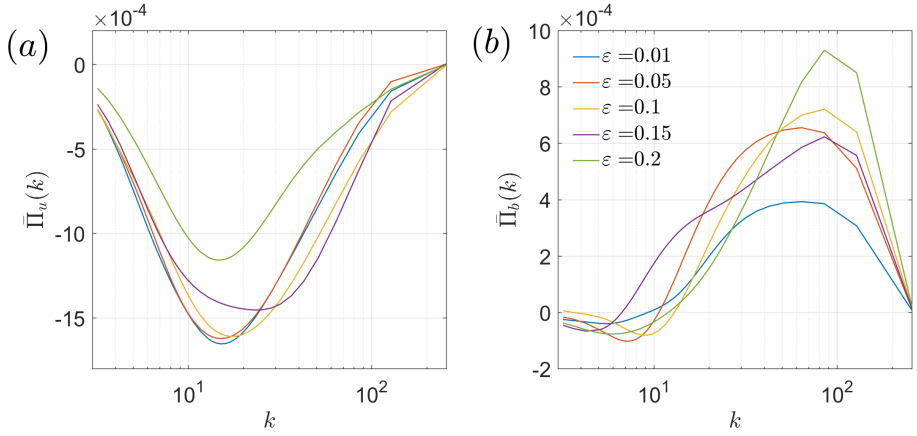


**Figure 7.** (Colour online) (a) Surface kinetic energy flux $\bar{\Pi}_u^l$ and (b) potential energy flux $\bar{\Pi}_b^l$ versus $k$ in the flows with different $\varepsilon$ at $T = 30$.

ated with the forward-cascading potential energy, while areas of downwelling exhibit an inverse cascade. This observation appears to be consistent with (Hakim et al., 2002)'s conclusion that the contraction of warm filaments develops faster than that of cold ones.

### 4.3 Finite-scale Lyapunov exponents

To study stirring in the SSG flows we compute trajectories of numerical particles in our flows. The trajectories can be used to obtain finite-scale Lyapunov exponents (FSLEs) which are a useful metric of stirring (d'Ovidio et al., 2004). FSLEs are inversely proportional to time $\tau$ it takes a pair of particles initially separated by a distance $\delta_i$ to reach a prescribed final separation $\delta_f$:

$$\lambda(x, y, t, \delta_i, \delta_f) = \frac{1}{\tau} \log \frac{\delta_f}{\delta_i}. \tag{28}$$

Trajectories of particles are computed by integrating velocity fields over time using the fourth-order Runge-Kutta scheme. The velocity at particle locations is obtained by a bilinear interpolation at each time step. Particles are initially seeded in between the nodes of the computational grid such that their smallest initial separation is half of the grid spacing, $\delta_i = 0.5\Delta x$. Each particle is surrounded by four neighboring particles in the shape of a diamond. The separations between particles in the diamond in x- and y-directions are calculated at each time step; when the maximum separation reaches $\delta_f$, the time $\tau$ is obtained. The velocity is integrated either forward or backward in time to obtain two sets of the exponents $\lambda_+$ and $\lambda_-$, respectively. High values of $\lambda_+$ indicate areas where particles separate from each other due to lateral divergence. High values of $\lambda_-$, on the other hand, indicate areas of convergence where particles accumulate.

Spatial distributions of FSLEs can be used for detecting the so-called Lagrangian structures, the structures formed by Lagrangian particles. High values of both exponents often manifest themselves as filament-like structures in the ocean(d'Ovidio et al., 2004; Calil & Richards, 2010; Siegelman et al., 2020). A typical spatial pattern of the exponents in our simulations is shown in Figure 8(b) where both $\lambda_+$ (yellow color) and $\lambda_-$ (blue color) are plotted together. It is an illustration of stirring by strong vortices. Cyclonic vortices created by cold patches (black color) create a fine structure of filaments wrapped around their cores. Two pairs of cyclones located in the part of the computational domain shown in Figure 8(b) create two figure-eight patterns where attracting lines (blue color) intersect repelling lines (yellow color) at a hyperbolic point in the area between the vortices. It is in this area the strain rate is as important as the relative vorticity. Two warm anticyclones (white color) do not seem to create distinct patterns of filaments in their cores but contribute to strain in the areas between them and other vortices.

Domain-averaged FSLEs can be used to identify regimes of dispersion at different scales. Here, we compute a spectrum of the mean exponent $\bar{\lambda} = 0.5(\lambda_+ + \lambda_-)$ averaged over the surface area of the domain. In this computation, the initial separation between the particles in diamond patterns was varied in a wide range between $\delta_i = \Delta x$ and $\delta_i = 110\Delta x$. The particles were followed until the separation between them reached a prescribed final value $\delta_f = \sqrt{2}\delta_i$ (Lacorata et al., 2001). $\bar{\lambda}$ as a function of $\delta_i$ is shown in Fig. 9 for simulations with different $\varepsilon$. Note that the range of dimensionless $\delta_i$ in Fig. 9 corresponds to the range of the dimensionless wavenumber, $k = L/2\delta_i$, from 256 down to 3 for comparison with the energy spectra in Fig. 5. The slope of the $\bar{\lambda}$ spectrum varies continuously with $\delta_i$ such that there is no extended interval where it remains constant. At the smallest scales up to approximately $\delta_i = 4\Delta x$ the spectrum is almost flat, $\bar{\lambda} \approx$ constant. The flat spectrum indicates that the distance between particle trajectories increases exponentially in time. At larger scales, the slope varies from approximately -1/2 to -2.

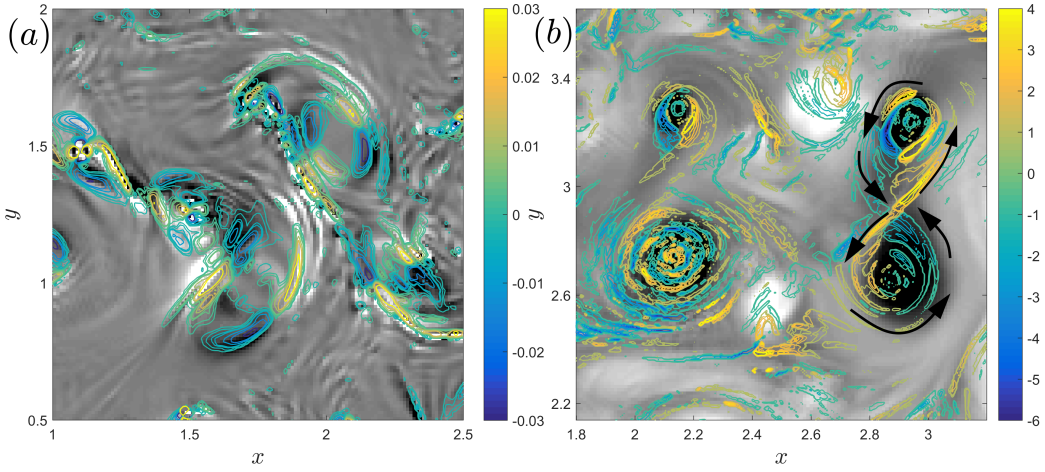


**Figure 8.** (Colour online) Typical patterns of the potential energy flux $\Pi_b^l(x,y)$ (a) and the FSLEs $\lambda_+$ and $\lambda_-$ (b) in the flows $\varepsilon = 0.1$. Contours of $\Pi_b^l(x,y)$ across wavenumber $k = 85$ are superposed over the vertical velocity field $w(x,y)$ (gray-scale) in the range between $-5 \times 10^{-3}$ and $5 \times 10^{-3}$. Contours of the FSLEs are superposed over the buoyancy field $b_s(x,y)$ (gray-scale) in the range between $-0.6$ and $0.6$. Black arrows indicate the direction of the velocity around one of the cyclone pairs.

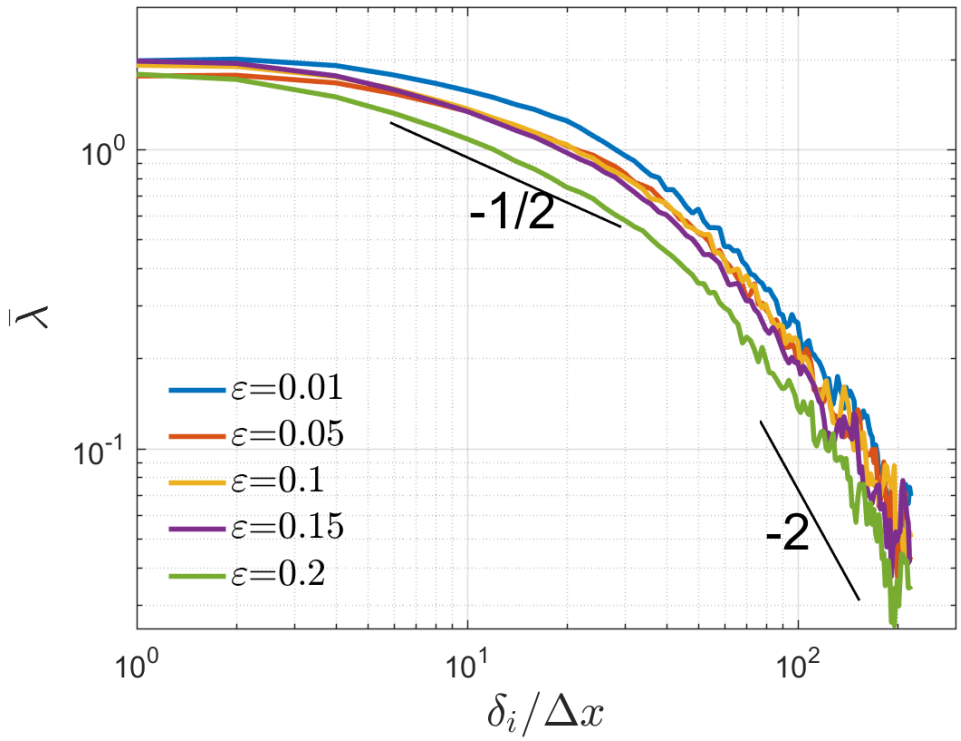


**Figure 9.** (Colour online) FSLE spectra for five simulations with different $\varepsilon$ at $T = 30$.

Scaling theory for turbulent flows where the kinetic energy spectrum is $\mathcal{K}_s(k) \propto k^{-\alpha}$ predicts the power-law scale dependence of the FSLE, $\bar{\lambda} \propto \delta_i^{-\beta}$, and the power-law time dependence of the separation between particles, $\delta^2(t) \propto t^{2/\beta}$ where $\beta = (3-\alpha)/2$ (Morel & Larceveque, 1974). These power-law equations are applicable when the kinetic energy spectrum is not too steep, $\alpha < 3$. In this case, the dispersion regime is local, the separation of particles at a certain scale is only determined by the velocity gradient components at the same scale. Otherwise, the dispersion regime is non-local; the power-law is not applicable and the separation between particles grows exponentially in time.

In our flows, $\alpha \approx 2$ at intermediate values of the wavenumber (Fig. 5). In this interval, a local dispersion regime with $\beta \approx 1/2$ is expected. The separation between particles grows quite fast, $\delta^2(t) \propto t^4$, and the regime can be called hyper-ballistic. $\beta$ then keeps increasing with $\delta_i$ up to $\beta = 2$. In this range, several distinct regimes of dispersion can be pointed out. When $\beta = 2/3$ the dispersion obeys the Richardson's law which describes another case of the hyper-ballistic dispersion where $\delta^2(t) \propto t^3$; in this case, the energy spectrum has Kolmogorov's -5/3 slope. When $\beta = 1$ and $\delta^2(t) \propto t^2$ the motion of particles is ballistic as if they move with constant speed away from one another. Finally, when $\beta = 2$ the regime is a normal diffusion, $\delta^2(t) \propto t$ is similar to that of the Brownian motion. In our flows, the normal diffusion is due to the scattering of particles by the energetic warm and cold eddies at large scales.

## 5 Conclusions

In this work, turbulent flows were simulated at different values of the Rossby number, $\varepsilon$, using the SSG model. The simulated flows exhibited typical ageostrophic effects, including a cyclone-anticyclone asymmetry with a cyclonic preference for vortices and an anticyclonic preference for filaments. The magnitude of the ageostrophic effects increased with $\varepsilon$ due to the increasing higher-order ageostrophic term in the SSG solution (Equation A7). As $\varepsilon$ increased from 0.01 to 0.2 between the simulations, the number of warm filaments on the surface increased, resulting in a surface warming trend.

The magnitude of the vertical velocity and, consequently, the lateral divergence also increased with $\varepsilon$. Vertical motions occurred mostly in small-scale filaments and at the periphery of vortices rather than in their cores. However, in all our simulations, the lateral divergence remained much smaller than the relative vorticity or the strain rate. This contrasted with the results of (Balwada et al., 2021), where the authors used primitive equations and obtained lateral divergence values comparable to those of relative vorticity and strain rate. We believe this difference is mainly due to the distinct forcing used in their simulations compared to buoyancy-only initial forcing in ours. Our results demonstrated a negative correlation between lateral divergence and relative vorticity, $\delta = -\bar{\sigma}/2\zeta$ (Figure 4). This indicates that cyclonic and anticyclonic motions are often associated with local convergence and divergence, respectively. This effect is most pronounced in strain-dominated areas where $\sigma > |\zeta|$.

Spectral analyses showed that the kinetic and potential energy spectra exhibited similar slopes, varying between -2.2 and -1.7 as $\varepsilon$ increased from 0.01 to 0.2. Notably, the latter value of the slope is approximately equal to -5/3, in agreement with previous SSG simulations by (Ragone & Badin, 2016) and SQG+1 simulations by (Capet et al., 2008). The similarity of the kinetic and potential energy spectra is a well-known feature of SQG turbulence, where it is caused by the thermal-wind coupling between the velocity field and the buoyancy field at the surface. In the SSG flow, this coupling seems largely unaffected by the inclusion of the ageostrophic component.

Spectra of gradient fields, including relative vorticity $\zeta$ and strain rate $\sigma$ (Figure 5(c)), were approximately flat in the wavenumber range where the kinetic energy slope

was approximately -2. The spectra of another gradient field, lateral divergence $\delta$, however, showed a maximum at a relatively large wavenumber $k_{max}$, which increased almost linearly with $\varepsilon$.

In addition to energy spectra, energy fluxes across different scales were computed. The fluxes showed that kinetic energy is transferred towards larger scales, constituting an inverse cascade. However, the cascade rate was not constant across scales; it reached a peak at a scale $l = 2\pi/k = 0.35$, corresponding to wavenumber $k = 18$. This scale roughly agreed with the typical distance between cold cyclones. Visual inspection of the flux fields showed that kinetic energy flux concentrated in and around cold cyclones (Figure 6(c)). Interestingly, the magnitude of the flux decreased as $\varepsilon$ increased, and the flows became more ageostrophic and three-dimensional. One of the effects slowing down the inverse cascade was warm filaments wrapping around cold cyclones, shielding them, and preventing mergers. Potential energy, on the other hand, cascaded forward towards smaller scales at all wavenumbers greater than $k \approx 20$. The potential energy flux was maximum at $k \approx 85$. Comparison of the flux with the vertical velocity field (Figure 8(a)) showed that the forward cascade was mainly associated with warm filaments created by upwelling. The magnitude of the potential energy flux increased with $\varepsilon$, a consequence of the growing number of filaments in ageostrophic flows.

To explore lateral stirring and dispersion of particles by eddies and filaments in our flows, we computed the trajectories of numerical particles and obtained forward and backward FSLEs. Inspection of the FSLE fields showed that interacting cold cyclones created Lagrangian coherent structures in between them (Figure 8(b)). The relative dispersion of particles was scale-dependent in our flows. To study the regimes of dispersion, mean FSLEs were computed for different initial separations of particles $\delta_i$. The results showed (Figure 9) that at the smallest scales, the relative dispersion of a pair of particles was exponential in time and non-local. At larger scales, the dispersion regime was local, and the mean FSLE, $\bar{\lambda}$, satisfied a power law, $\bar{\lambda} \propto \delta_i^{-\beta}$, where $\beta$ varied smoothly from approximately 1/2 to 2 with increasing $\delta_i$. The variation of $\beta$ reflected a transition from a hyper-ballistic dispersion regime ($\beta \approx 1/2$) to Richardson's dispersion ($\beta \approx 2/3$) and then to a ballistic regime ($\beta \approx 1$) and finally to normal diffusion ($\beta \approx 2$). The smooth transition of $\beta$ from 1/2 to 2 was a robust feature in all our simulations for different $\varepsilon$. A similar transition of the exponent $\beta$ was previously found in SQG+1 turbulence (Maalouly et al., 2023, their figure 4) and observed for drifters in the Antarctic Circumpolar Current (Balwada et al., 2021, their figure 9).

## Appendix A Solution of the SSG equations

Eq. (18), can be written in non-dimensional form as:

$$\nabla^2 \Phi = \varepsilon D\Phi, \tag{A1}$$

where $\nabla^2$ is the three-dimensional Laplacian operator in the geostrophic space and

$$D\Phi = \frac{\partial^2 \Phi}{\partial X^2}\frac{\partial^2 \Phi}{\partial Y^2} - \left(\frac{\partial^2 \Phi}{\partial X \partial Y}\right)^2 \tag{A2}$$

is the nonlinear differential operator. Horizontal Fourier transform can then be used to obtain a forced Helmholtz equation in the vertical direction which can be solved numerically by iteration:

$$\left(\frac{\partial}{\partial Z^2} - k^2\right)\tilde{\Phi}^{(n)} = \varepsilon \tilde{D}\Phi^{(n-1)}. \tag{A3}$$

The iteration is performed for each wavevector $\boldsymbol{k} = (k_X, k_Y)$ in the (geostrophic) wavenumber space. Boundary conditions Eq. (4) can be written as:

$$\begin{aligned} \frac{\partial \tilde{\Phi}(\boldsymbol{k}, Z)}{\partial Z} &= \tilde{b}_s \quad \text{at} \quad Z = 0, \\ \frac{\partial \tilde{\Phi}(\boldsymbol{k}, Z)}{\partial Z} &= 0 \quad \text{at} \quad Z = -1. \end{aligned} \tag{A4}$$

Equation (A3) with the boundary conditions Eq. (A4) has a solution in the form of the Green's function:

$$\tilde{\Phi}^{(n)}(\boldsymbol{k}, Z) = \tilde{b}_s(\boldsymbol{k}, t) G_k(Z, 0) + \varepsilon \int_{-1}^{0} G_k(Z, Z') \tilde{D\Phi}^{(n-1)}(\boldsymbol{k}, Z') dZ' \tag{A5}$$

where

$$G_k(Z, Z') = \begin{cases} \cosh(kZ) \cosh[k(Z'+1)]/(k \cdot \sinh k), & Z \geq Z' \\ \cosh[k(Z+1)] \cosh(kZ')/(k \cdot \sinh k), & Z < Z'. \end{cases} \tag{A6}$$

The first-order approximation of the solution is given by

$$\tilde{\Phi}^{(1)}(\boldsymbol{k}, Z) = \tilde{\Phi}^{(0)}(\boldsymbol{k}, Z) + \varepsilon \int_{-1}^{0} G_k(Z, Z') \tilde{D\Phi}^{(0)}(\boldsymbol{k}, Z') dZ' \tag{A7}$$

where the zeroth-order approximation

$$\tilde{\Phi}^{(0)}(\boldsymbol{k}, Z) = \tilde{b}_s(\boldsymbol{k}, t) G_k(Z, 0) = \frac{\cosh[(Z+1)k]}{k \sinh(k)} \tilde{b}_s(\boldsymbol{k}, t) \tag{A8}$$

is the SQG solution Eq. (7). Following (Ragone & Badin, 2016) who showed that when $\varepsilon$ is small, the first-order approximation provides reasonably accuracy we use Eq. (A7) for the numerical solution of the SSG problem.

Buoyancy, $b_s$, is a conserved quantity such that:

$$\frac{db_s}{dt} = \frac{\partial b_s}{\partial t} + u_g \frac{\partial b_s}{\partial X} + v_g \frac{\partial b_s}{\partial Y} = 0. \tag{A9}$$

Given an initial buoyancy perturbation field $b_s(X, Y)$ in the geostrophic space, one can calculate the Bernoulli function $\Phi(X, Y)$ using Equation (A5). Geostrophic velocity, $(u_g, v_g)$, is then given by Eq. (11). Finally Eq. (A9) can be marched in time numerically.

## Appendix B Vertical velocity

In the SSG model, a re-scaled vertical velocity $w^* = J \cdot w$ can be obtained from the so-called "$\Omega$-equation" (Hoskins & West, 1979; Ragone & Badin, 2016):

$$\frac{\partial^2 w^*}{\partial X^2} + \frac{\partial^2 w^*}{\partial Y^2} + \frac{\partial^2 w^*}{\partial Z^2} = -2\varepsilon \nabla \cdot \boldsymbol{Q}, \tag{B1}$$

where

$$J = 1 - \varepsilon \left( \frac{\partial v_g}{\partial X} - \frac{\partial u_g}{\partial Y} \right) \tag{B2}$$

is the re-scaling factor and

$$\boldsymbol{Q} = (Q_1, Q_2) = \left( \frac{\partial u_g}{\partial X} \frac{\partial b}{\partial X} + \frac{\partial v_g}{\partial X} \frac{\partial b}{\partial Y}, \frac{\partial u_g}{\partial Y} \frac{\partial b}{\partial X} + \frac{\partial v_g}{\partial Y} \frac{\partial b}{\partial Y} \right) \tag{B3}$$

is the forcing vector. These two quantities can be calculated using Eqs. (11) and (A7). Applying Fourier transform in the horizontal direction, Eq. (B1) can be written as

$$-k^2 \tilde{w}^* + \frac{\partial^2 \tilde{w}^*}{\partial Z^2} = \tilde{Q}(k, Z), \tag{B4}$$

where $\tilde{Q}(k, Z)$ is the Fourier transform of the RHS of Eq. (B1). For each geostrophic wavenumber $k = \sqrt{k_X^2 + k_Y^2} \neq 0$, Eq. (B4) subject to the boundary conditions $\tilde{w}^* = 0$ at $Z = 0$ and $Z = -1$ has the following solution:

$$\tilde{w}^*(k, Z) = \exp(kZ) \int_0^Z \delta_3(k, z')dz' - \exp(-kZ) \int_0^Z \delta_4(k, z')dz' + 2\frac{\delta_2(k)}{\delta_1(k)} \sinh(kZ) \quad \text{(B5)}$$

where

$$\delta_1(k) = -2\sinh(k), \quad \text{(B6a)}$$

$$\delta_2(k) = \exp(k) \int_0^{-1} \delta_4 dz' - \exp(-k) \int_0^{-1} \delta_3 dz', \quad \text{(B6b)}$$

$$\delta_3(k, z') = \exp(-kz')\frac{\tilde{Q}(k, z')}{2k}, \quad \text{(B6c)}$$

$$\delta_4(k, z') = \exp(kz')\frac{\tilde{Q}(k, z')}{2k}. \quad \text{(B6d)}$$

The above analytical solution is provided by the symbolic math toolbox in MATLAB. Inverse Fourier transform of Eq. (B5) then gives the vertical velocity in the geostrophic coordinates, $w(X, Y, Z)$.

## 3 Availability Statement

The code for the SSG model is available at: `github.com/zy-gdou/` The Matlab figures, the data and codes used for creating the figures are available from the ZENODO repository (https://doi.org/10.5281/zenodo.10431740).

**Acknowledgments**
Yang Zhang and Shuwen Zhang are supported by National Natural Science Foundation of China grants 92158201 and 42376001; Yakov Afanasyev is supported by the NSERC grant RGPIN 2019-04957.

## References

Afanasyev, Y. D., & Craig, J. D. (2013). Rotating shallow water turbulence: Experiments with altimetry. *Physics of Fluids*, *25*(10). doi: 10.1063/1.4826477

Aluie, H., Hecht, M., & Vallis, G. K. (2018). Mapping the energy cascade in the North Atlantic Ocean: The coarse-graining approach. *Journal of Physical Oceanography*, *48*(2), 225–244. doi: 10.1175/JPO-D-17-0100.1

Arakawa, A. (1966). Computational design for long-term numerical integration of the equations of fluid motion: Two-dimensional incompressible flow. Part I. *Journal of Computational Physics*, *135*(2), 103–114.

Balwada, D., LaCasce, J. H., & Speer, K. G. (2016). Scale-dependent distribution of kinetic energy from surface drifters in the Gulf of Mexico. *Geophysical Research Letters*, *43*(20), 10,856–10,863. doi: 10.1002/2016GL069405

Balwada, D., LaCasce, J. H., Speer, K. G., & Ferrari, R. (2020). Relative Dispersion in the Antarctic Circumpolar Current. *Journal of Physical Oceanography*, *51*(2), 553–574. doi: 10.1175/jpo-d-19-0243.1

Balwada, D., Xiao, Q., Smith, S., Abernathey, R., & Gray, A. R. (2021). Vertical fluxes conditioned on vorticity and strain reveal submesoscale ventilation. *Journal of Physical Oceanography*(2018), 2883–2901. doi: 10.1175/jpo-d-21-0016.1

Barkan, R., Molemaker, M. J., Srinivasan, K., McWilliams, J. C., & D'Asaro, E. A. (2019). The role of horizontal divergence in submesoscale frontogenesis. *Journal of Physical Oceanography*, *49*(6), 1593 - 1618. Retrieved from `https://`

journals.ametsoc.org/view/journals/phoc/49/6/jpo-d-18-0162.1.xml doi: https://doi.org/10.1175/JPO-D-18-0162.1

Blumen, W. (1978). Uniform Potential Vorticity Flow: Part I. Theory of Wave Interactions and Two-Dimensional Turbulence. *Journal of the Atmospheric Sciences*, *35*(5), 774–783. doi: 10.1175/1520-0469(1978)035⟨0774:upvfpi⟩2.0.co;2

Boyd, J. P. (1992). kinetic energy spectrum of a frontogenesis. *Journal of the Atmospheric Sciences*, *49*(2), 128–139.

Calil, P. H., & Richards, K. J. (2010). Transient upwelling hot spots in the oligotrophic North Pacific. *Journal of Geophysical Research: Oceans*, *115*(2), 1–20. doi: 10.1029/2009JC005360

Capet, X., Klein, P., Hua, B. L., Lapeyre, G., & McWilliams, J. C. (2008). Surface kinetic energy transfer in surface quasi-geostrophic flows. *Journal of Fluid Mechanics*, *604*, 165–174. doi: 10.1017/S0022112008001110

Carton, X., Ciani, D., Verron, J., Reinaud, J., & Sokolovskiy, M. (2016). Vortex merger in surface quasi-geostrophy. *Geophysical and Astrophysical Fluid Dynamics*, *110*(1), 1–22. Retrieved from http://dx.doi.org/10.1080/03091929.2015.1120865 doi: 10.1080/03091929.2015.1120865

Chassignet, E. P., & Xu, X. (2017). Impact of horizontal resolution (1/12° to 1/50°) on Gulf Stream separation, penetration, and variability. *Journal of Physical Oceanography*, *47*(8), 1999–2021. doi: 10.1175/JPO-D-17-0031.1

Chavanne, C., Flament, P., & Gurgel, K. W. (2010). Interactions between a submesoscale anticyclonic vortex and a front. *Journal of Physical Oceanography*, *40*(8), 1802–1818. doi: 10.1175/2010JPO4055.1

Chen, S., Ecke, R. E., Eyink, G. L., Rivera, M., Wan, M., & Xiao, Z. (2006). Physical mechanism of the two-dimensional inverse energy cascade. *Physical Review Letters*, *96*(8). doi: 10.1103/PhysRevLett.96.084502

Constantin, P., Lai, M. C., Sharma, R., Tseng, Y. H., & Wu, J. (2012). New numerical results for the surface quasi-geostrophic equation. *Journal of Scientific Computing*, *50*(1), 1–28. doi: 10.1007/s10915-011-9471-9

Davies, H. C., & Muller, J. C. (1988, jul). Detailed description of deformation-induced semi-geostrophic frontogenesis. *Quarterly Journal of the Royal Meteorological Society*, *114*(483), 1201–1219. doi: 10.1002/qj.49711448303

d'Ovidio, F., Fernández, V., Hernández-García, E., & López, C. (2004). Mixing structures in the mediterranean sea from finite-size lyapunov exponents. *Geophysical Research Letters*, *31*(17). Retrieved from https://agupubs.onlinelibrary.wiley.com/doi/abs/10.1029/2004GL020328 doi: https://doi.org/10.1029/2004GL020328

Eliassen, A. (1948). The quasi-static equations of motion. *Geofys. Publ.*, *17*, 5–44.

Fjørtoft, R. (1962). On the integration of a system of geostrophically balanced prognostic equations. In *In proceedings of the international symposium on numerical weather prediction* (pp. 153–159). Meteorological Society of Japan.

Germano, M. (1992). Turbulence: the filtering approach. *Journal of Fluid Mechanics*, *238*, 325–336.

Griffa, A., Lumpkin, R., & Veneziani, M. (2008). Cyclonic and anticyclonic motion in the upper ocean. *Geophysical Research Letters*, *35*(1), 1–5. doi: 10.1029/2007GL032100

Gula, J., Molemaker, M. J., & McWilliams, J. C. (2016). Submesoscale dynamics of a Gulf Stream frontal eddy in the South Atlantic Bight. *Journal of Physical Oceanography*, *46*(1), 305–325. doi: 10.1175/JPO-D-14-0258.1

Hakim, G. J., Snyder, C., & Muraki, D. J. (2002). A new surface model for cyclone-anticyclone asymmetry. *Journal of the Atmospheric Sciences*, *59*(16), 2405–2420. doi: 10.1175/1520-0469(2002)059⟨2405:ANSMFC⟩2.0.CO;2

Held, I. M., Pierrehumbert, R. T., Garner, S. T., & L.Swanson, K. (1994). Surface Quasi-Geostrophic Dynamics. *Journal of Fluid Mechanics*, *282*(June 2014), 1–20. doi: 10.1017/S0022112095000012

Hoskins, B. J. (1975). Geostrophic Momentum Approximation and the Semi-Geostrophic Equations. *Journal of the Atmospheric Sciences*, *32*(2), 233–242. doi: 10.1175/1520-0469(1975)032⟨0233:TGMAAT⟩2.0.CO;2

Hoskins, B. J. (1976). Baroclinic waves and frontogenesis Part I: Introduction and Eady waves. *Quarterly Journal of the Royal Meteorological Society*, *102*(431), 103–122. doi: 10.1002/qj.49710243109

Hoskins, B. J., & Bretherton, F. P. (1972). Atmospheric Frontogenesis Models: Mathematical Formulation and Solution. *Journal of the Atmospheric Sciences*, *29*(1), 11–37. doi: 10.1175/1520-0469(1972)029⟨0011:afmmfa⟩2.0.co;2

Hoskins, B. J., & Draghici, I. (1977, dec). The Forcing of Ageostrophic Motion According to the Semi-Geostrophic Equations and in an Isentropic Coordinate Model. *Journal of the Atmospheric Sciences*, *34*(12), 1859–1867. Retrieved from `https://journals.ametsoc.org/view/journals/atsc/34/12/1520-0469_1977_034_1859_tfoama_2_0_co_2.xml?tab_body=pdfhttp://journals.ametsoc.org/doi/10.1175/1520-0469(1977)034%3C1859:TFOAMA%3E2.0.CO;2` doi: 10.1175/1520-0469(1977)034⟨1859:TFOAMA⟩2.0.CO;2

Hoskins, B. J., & West, N. V. (1979). Baroclinic waves and frontogenesis. Part II: Uniform potential vorticity jet flows-cold and warm fronts. *Journal of Atmospheric Sciences*, *36*(9), 1663–1680.

Hou, T. Y., & Li, R. (2007). Computing nearly singular solutions using pseudo-spectral methods. *Journal of Computational Physics*, *226*(1), 379–397. doi: 10.1016/j.jcp.2007.04.014

Isern-Fontanet, J., Chapron, B., Lapeyre, G., & Klein, P. (2006). Potential use of microwave sea surface temperatures for the estimation of ocean currents. *Geophysical Research Letters*, *33*(24), 1–5. doi: 10.1029/2006GL027801

Jing, Z., Fox-Kemper, B., Cao, H., Zheng, R., & Du, Y. (2021). Submesoscale fronts and their dynamical processes associated with symmetric instability in the northwest pacific subtropical ocean. *Journal of Physical Oceanography*, *51*(1), 83–100. doi: 10.1175/JPO-D-20-0076.1

Kimura, Y., & Herring, J. R. (2001). Gradient enhancement and filament ejection for a non-uniform elliptic vortex in two-dimensional turbulence. *Journal of Fluid Mechanics*, *439*, 43-56.

Klein, P., Hua, B. L., Lapeyre, G., Capet, X., Le Gentil, S., & Sasaki, H. (2008). Upper ocean turbulence from high-resolution 3D simulations. *Journal of Physical Oceanography*, *38*(8), 1748–1763. doi: 10.1175/2007JPO3773.1

Lacorata, G., Aurell, E., & Vulpiani, A. (2001). Drifter dispersion in the adriatic sea: Lagrangian data and chaotic model. *Annales Geophysicae*, *19*(1), 121–129. Retrieved from `https://angeo.copernicus.org/articles/19/121/2001/` doi: 10.5194/angeo-19-121-2001

Lapeyre, G. (2017). Surface Quasi-Geostrophy. *Fluids*, *2*(1). doi: 10.3390/fluids2010007

Lapeyre, G., & Klein, P. (2006a). Dynamics of the upper oceanic layers in terms of surface quasigeostrophy theory. *Journal of Physical Oceanography*, *36*(2), 165–176. doi: 10.1175/JPO2840.1

Lapeyre, G., & Klein, P. (2006b). Impact of the small-scale elongated filaments on the oceanic vertical pump. *Journal of Marine Research*, *64*(6), 835–851. doi: 10.1357/002224006779698369

Maalouly, M., Lapeyre, G., Cozian, B., Mompean, G., & Berti, S. (2023). *Particle dispersion and clustering in surface ocean turbulence with ageostrophic dynamics.*

Mahadevan, A., & Tandon, A. (2006). An analysis of mechanisms for submesoscale vertical motion at ocean fronts. *Ocean Modelling*, *14*(3-4), 241–256. doi: 10.1016/j.ocemod.2006.05.006

McWilliams, J. C. (2016). Submesoscale currents in the ocean. *Proceedings of the Royal Society A: Mathematical, Physical and Engineering Sciences*, *472*(2189).

doi: 10.1098/rspa.2016.0117

McWilliams, J. C., & Gent, P. R. (1980). Intermediate models of planetary circulations in the atmosphere and ocean. *Journal of the Atmospheric Sciences*, *37*(8), 1657–1678. doi: 10.1175/1520-0469(1980)037⟨1657:IMOPCI⟩2.0.CO;2

Mensa, J. A., Timmermans, M. L., Kozlov, I. E., Williams, W. J., & Özgökmen, T. M. (2018). Surface Drifter Observations From the Arctic Ocean's Beaufort Sea: Evidence for Submesoscale Dynamics. *Journal of Geophysical Research: Oceans*, *123*(4), 2635–2645. doi: 10.1002/2017JC013728

Morel, P., & Larceveque, M. (1974). Relative dispersion of constant–level balloons in the 200–mb general circulation. *Journal of Atmospheric Sciences*, *31*(8), 2189 - 2196. Retrieved from `https://journals.ametsoc.org/view/journals/atsc/31/8/1520-0469_1974_031_2189_rdocbi_2_0_co_2.xml` doi: https://doi.org/10.1175/1520-0469(1974)031⟨2189:RDOCBI⟩2.0.CO;2

Munk, W. (2000). Spirals on the sea. *Proceedings of the Royal Society of London. Series A: Mathematical, Physical and Engineering Sciences*, *456*, 1217–1280. doi: 10.3989/scimar.2001.65s2193

Pearson, J., Fox-Kemper, B., Barkan, R., Choi, J., Bracco, A., & Mcwilliams, J. C. (2019). Impacts of convergence on structure functions from surface drifters in the Gulf of Mexico. *Journal of Physical Oceanography*, *49*(3), 675–690. doi: 10.1175/JPO-D-18-0029.1

Qiu, B., Chen, S., Klein, P., Ubelmann, C., Fu, L. L., & Sasaki, H. (2016). Reconstructability of three-dimensional upper-ocean circulation from SWOT sea surface height measurements. *Journal of Physical Oceanography*, *46*(3), 947–963. doi: 10.1175/JPO-D-15-0188.1

Ragone, F., & Badin, G. (2016). A study of surface semi-geostrophic turbulence: Freely decaying dynamics. *Journal of Fluid Mechanics*, *792*, 740–774. doi: 10.1017/jfm.2016.116

Roullet, G., & Klein, P. (2010). Cyclone-anticyclone asymmetry in geophysical turbulence. *Physical Review Letters*, *104*(21), 28–31. doi: 10.1103/PhysRevLett.104.218501

Ruiz, S., Claret, M., Pascual, A., Olita, A., Troupin, C., Capet, A., ... Mahadevan, A. (2019). Effects of Oceanic Mesoscale and Submesoscale Frontal Processes on the Vertical Transport of Phytoplankton. *Journal of Geophysical Research: Oceans*, *124*(8), 5999–6014. doi: 10.1029/2019JC015034

Shcherbina, A. Y., D'Asaro, E. A., Lee, C. M., Klymak, J. M., Molemaker, M. J., & McWilliams, J. C. (2013). Statistics of vertical vorticity, divergence, and strain in a developed submesoscale turbulence field. *Geophysical Research Letters*, *40*(17), 4706–4711. doi: 10.1002/grl.50919

Siegelman, L., Klein, P., Rivière, P., Thompson, A. F., Torres, H. S., Flexas, M., & Menemenlis, D. (2020). Enhanced upward heat transport at deep submesoscale ocean fronts. *Nature Geoscience*, *13*(1), 50–55. doi: 10.1038/s41561-019-0489-1

Thomas, L. N., Tandon, A., & Mahadevan, A. (2008). Submesoscale processes and dynamics. *Geophysical Monograph Series*, *177*, 17–38. doi: 10.1029/177GM04

Traon, P. Y. L., Klein, P., Hua, B. L., & Dibarboure, G. (2008). Do altimeter wavenumber spectra agree with the interior or surface quasigeostrophic theory? *Journal of Physical Oceanography*, *38*(5), 1137–1142. doi: 10.1175/2007JPO3806.1

Tulloch, R., & Smith, K. S. (2006). A theory for the atmospheric energy spectrum: Depth-limited temperature anomalies at the tropopause. *Proceedings of the National Academy of Sciences of the United States of America*, *103*(40), 14690–14694. doi: 10.1073/pnas.0605494103

Xiao, Z., Wan, M., Chen, S., & Eyink, G. L. (2009). Physical mechanism of the inverse energy cascade of two-dimensional turbulence: A numerical investigation. *Journal of Fluid Mechanics*, *619*(February 2016), 1–44. doi:

643 10.1017/S0022112008004266
644 Zhang, Y., & Afanasyev, Y. D. (2016). Baroclinic turbulence on the polar $\beta$-plane in
645 the rotating tank: Down to submesoscale. *Ocean Modelling*, *107*, 151–160. doi:
646 10.1016/j.ocemod.2016.09.013